ADVANCED ENERGY MATERIALS
www.advenergymat.de

Tailoring Molecular Space to Navigate Phase Complexity in Cs-Based Quasi-2D Perovskites via Gated-Gaussian-Driven High-Throughput Discovery

Minsub Um, Sheryl L. Sanchez, Hochan Song, Benjamin J. Lawrie, Hyungju Ahn, Sergei V. Kalinin, Yongtao Liu, Hyosung Choi,* Jonghee Yang,* and Mahshid Ahmadi**

Cesium-based quasi-2D halide perovskites (HPs) offer promising functionalities and low-temperature manufacturability, suited to stable tandem photovoltaics. However, the chemical interplays between the molecular spacers and the inorganic building blocks during crystallization cause substantial phase complexities in the resulting matrices. To successfully optimize and implement the quasi-2D HP functionalities, a systematic understanding of spacer chemistry, along with the seamless navigation of the inherently discrete molecular space, is necessary. Herein, by utilizing high-throughput automated experimentation, the phase complexities in the molecular space of quasi-2D HPs are explored, thus identifying the chemical roles of the spacer cations on the synthesis and functionalities of the complex materials. Furthermore, a novel active machine learning algorithm leveraging a two-stage decision-making process, called gated Gaussian process Bayesian optimization is introduced, to navigate the discrete ternary chemical space defined with two distinctive spacer molecules. Through simultaneous optimization of photoluminescence intensity and stability that "tailors" the chemistry in the molecular space, a ternary-compositional quasi-2D HP film realizing excellent optoelectronic functionalities is demonstrated. This work not only provides a pathway for the rational and bespoke design of complex HP materials but also sets the stage for accelerated materials discovery in other multifunctional systems.

1. Introduction

Halide perovskites (HPs) are now leading materials pioneering photovoltaic (PV) technologies, owing to their simple solution processibility and excellent optoelectronic functionality. Among them, inorganic Cs-based HPs, where volatile methylammonium is excluded, are anticipated to be advantageous to thermal stability. Also, it offers a relatively wide bandgap of ≈1.7–1.8 eV that is desired for front cell in tandem PV applications,[1–4] while excluding substantial bromine incorporation that compromises bandgap stability via halide segregation.[5,6] However, thermodynamically, the synthesis of the photoactive α-$CsPbI_3$ phase requires high temperatures over 325 °C.[7,8] Such high temperature is incompatible with the organic-based hole-transport materials, thereby realizing p-i-n type PVs – chemically more stable and a conventional architecture for tandem PV application – difficult.

M. Um, J. Yang
Department of Chemistry
Yonsei University
Seoul 03722, Republic of Korea
E-mail: jhyang@yonsei.ac.kr

S. L. Sanchez, S. V. Kalinin, M. Ahmadi
Institute for Advanced Materials and Manufacturing
Department of Materials Science and Engineering
The University of Tennessee
Knoxville, TN 37996, USA
E-mail: mahmadi3@utk.edu

H. Song, H. Choi
Department of Chemistry
Research Institute for Natural Sciences and Research Institute for Convergence of Basic Science
Hanyang University
Seoul 04763, Republic of Korea
E-mail: hschoi202@hanyang.ac.kr

B. J. Lawrie, Y. Liu
Center for Nanophase Materials Sciences
Oak Ridge National Laboratory
Oak Ridge, TN 37831, USA
E-mail: liuy3@ornl.gov

B. J. Lawrie
Materials Science and Technology Division
Oak Ridge National Laboratory
Oak Ridge, TN 37831, USA

H. Ahn
Pohang Accelerator Laboratory
POSTECH
Pohang 37673, Republic of Korea

The ORCID identification number(s) for the author(s) of this article can be found under https://doi.org/10.1002/aenm.202404655

DOI: 10.1002/aenm.202404655

Dimensional confinement of HP lattices via surface coordination of large molecular spacers allows for the formation of distinctive 2D HP structures with various unit thicknesses of inorganic octahedra sheets (described as *n*), called quasi-2D HPs. The quasi-2D HPs offer more thermodynamically feasible synthesizability, enabling crystallization at relatively lower temperatures while not compromising the overall bandgap of the materials system with respect to 3D counterparts.[9–11] Furthermore, the molecular spacers coordinated to the quasi-2D HP surface improve the stability of the HP lattices, as it can act as a protection layer against environmental stressors (e.g., oxygen and moisture).[12–14]

A crucial challenge to fully exploit the quasi-2D HPs to optoelectronic applications lies in the concurrent emergence of multiple quasi-2D HP phases and their spatial distributions in the synthesized film matrices. Primarily, this is caused by adopting the nonequilibrium fabrication processing, though it is optimally compatible with manifesting a fairly homogeneous 3D HP matrix.[15–17] But more importantly, profound chemical interactions among the spacer cations, inorganic building blocks, and even solvents can manifest different crystallization dynamics and/or energetic pathways for each phase.[18–23] Thus, a comprehensive understanding of the supramolecular interaction is vital for resolving such phase complexities in quasi-2D HPs, thereby realizing bespoke manipulation and subsequent utilization of the complex materials for optoelectronic applications.

In fact, the chemical variability of spacer cations offers an infinite molecular space, making the systematic and comprehensive investigation of the supramolecular interaction difficult. Particularly, due to the coexistence and interplays of multiple physicochemical parameters of molecular spacer affecting HP crystallizations, manual exploration to resolve such a multifaceted problem is extremely challenging. Moreover, the chemistry in the vast molecular spaces is – inherently – discrete, rather than continuous landscapes. Thus, for optimizing the optoelectronic functionalities of the quasi-2D HPs, seamless navigation of such intricate chemical space is necessary, which is also difficult based on the classical, single-directional process refinement techniques.

Instead, extensive efforts to the quasi-2D HPs have been focused on utilizing them toward optoelectronic applications, particularly prioritizing the development of high-performance and stable devices. Thus, the exploration of the genuine roles of spacer cations in the materials system remains elusive so far. That is, a legitimate consensus on selecting optimal spacers and/or chemical compositions, as well as the fundamental insights into designing functional materials are still lacking.

In this work, we employ a high-throughput automated experimental workflow to effectively explore the chemical space associated with phase complexities, including phase emergence behaviors, in quasi-2D HP films,[13,14,24–29] defined by the spacer cations. Here, five primitive 2D HP systems employing spacer molecules with distinctive physicochemical properties are selected: *n*-butylammonium (BA), butane-1,4-diammonium (BDA), thiopheneethylammonium (ThEA), and 3,3-diphenylpropylammonium (DPA). These cations represent key aspects in the chemical space – including molecular sizes, shapes, molecular weights and dipole moments – of the molecules. By combinatorial mixing them with 3D $CsPbI_3$, the spacer-dependent phase emergence behaviors and stability of the low-temperature (<100 °C) processed film matrices are systematically assessed.

Multiple features strongly associated with the chemistry of spacer cations were identified. It is found that the use of a spacer with phenyl rings manifests stable 3D-like phases – high-*n* 2D HP structures where the surface coordinated spacers protect 3D $CsPbI_3$ lattice, which is failed to realize by employing thiophene ring or short alkyl chain spacers. This allows for the construction of stable HP film matrices that render an optimal bandgap of ≈1.8 eV. Such discrepancy is likely attributed to the difference in geometric symmetry for spacer-precursor chemical interaction. Note that the HP matrix with bulky DPA offers uneven surface morphology with segmented 3D-like HP crystallites compromising charge transport upon device application, though it exhibits outstanding phase stability.[16,30] Additionally, in contrast to the Ruddlesden–Popper (RP) type HPs that typically render severe 2D/3D phase separation along the vertical direction,[31,32] incorporation of Dion–Jacobson (DJ) type perovskite (i.e., $BDAPbI_4$) homogenizes the vertical phase distributions. These observations collectively reveal the importance of spacer chemistry for synthesizing quasi-2D HP matrices.

Inspired by the comprehensive observations via high-throughput experimentation, it is envisaged that a new quasi-2D HP matrix deploying benefits of each binary system can be designed via compositional mixing of both RP- and DJ-type 2D HP endmembers (i.e., PEA_2PbI_4 and $BDAPbI_4$, respectively) in a ternary system. Here, by developing and deploying a gated Gaussian process Bayesian optimization (Gated-GPBO), we navigate chemistry in such intricate and discrete molecular space and identify optimal compositions offering ideal bandgap with minimized phase inhomogeneities and local phase distributions. Indeed, the p-i-n type PVs employing the quasi-2D HP film – tailored by Gated-GPBO – exhibit improved performances than those deduced by grid-search, thus effectively identifying optimal compositions directed to device-applicable films at the low-temperature fabrication process. This clearly shows the powerfulness of the Gated-GPBO for the exploration of complex materials systems. Collectively, this work provides a new research workflow not only uncovering fundamental insights into the complex quasi-2D HP system but also presenting design principles for bespoke materials design and functionality manipulations toward sustainable applications.

2. Results and Discussion

2.1. Exploration of Spacer-Dependent Phase Emergence Behaviors in Quasi-2D HPs

Differences in molecular structure bestow different chemical properties on the spacer cations. For the synthesis of quasi-2D HPs, this in turn manifests notable differences in chemical interactions with other neighboring chemical species, which profoundly tunes the crystallization behaviors, stability, and other functionalities of the matrices. While control over such behaviors is crucial for designing functional materials, understanding such multi-dimensional properties in the complex materials system merely with classical batch-type investigation workflow falls short of the efficiency and insight needed for advanced

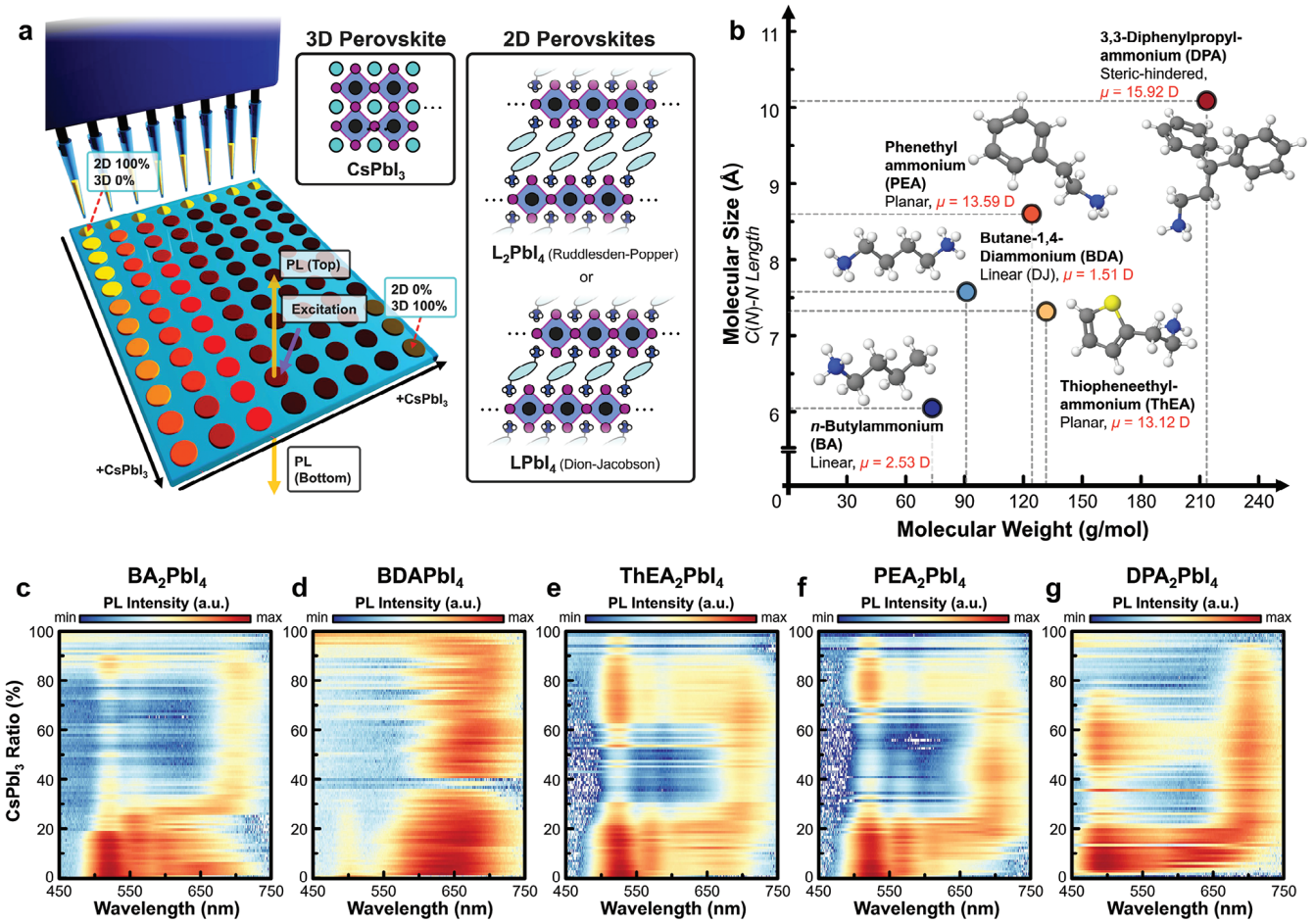

Figure 1. a) Schematic illustrating a high-throughput automated synthesis of quasi-2D HP film arrays with a pipetting-robot system. b) A chemical space of molecular spacers in this study. c–g) Composition-dependent top-surface PL spectra of the quasi-2D HP films having different spacer cations, showing differences in phase emergence behaviors: c) BA, d) BDA, e) ThEA, f) PEA, and g) DPA, respectively.

materials design. Specifically, such manual exploration requires a long and intricate exploration loop, as well as expensive costs. Thus, the progress is deemed to be slow, highly attributed to the difficulty in accurate decision-making from limited information at each stage.[33]

To systematically explore the spacer-dependent phase emergence behaviors in the corresponding quasi-2D HPs, we utilize a high-throughput automated experimental workflow.[14,27,29] Our designed workflow allows maximal acceleration of the synthesis–characterization–analysis cycle with much cheaper costs, enabled by the incorporation of rapid characterization methods and easy-to-interpret machine learning (ML) methods in the discovery loop. Here, the precursor solutions with different 2D:3D composition ratios – prepared via combinatorial mixing of 3D $CsPbI_3$ and respective 2D HP precursors, as shown in Figure S1 (Supporting Information) – are drop-casted onto the glass substrates. Subsequent thermal annealing at 95 °C allows for the synthesis of quasi-2D HP film arrays with the respective spacer cations. The resulting film arrays are quickly transferred to an optical reader to collect photoluminescence spectra from both the top and bottom surfaces over time. This allows us to identify the distinct phase emergence behaviors and vertical phase inhomogeneities, and assess their stabilities in each quasi-2D HP combinatorial library (**Figure 1a**). Here, we select five representative spacer cations as precursors: BA, BDA, ThEA, PEA, and DPA. In contrast to BA with a short alkyl chain, PEA, ThEA and DPA have one or two aromatic rings in the corresponding molecular structures, allowing for understanding the role of aromatic rings in phase emergence behaviors and stabilities; ThEA and DPA respectively provide additional insights into the chemical impact of heterocycle and the number of the aromatic ring on the phase growth of quasi-2D HPs. Also, BDA represents the phase growth features of DJ-type perovskite. Overall, this exploration allows us to discover the intrinsically optimal composition and spacer molecules for designing the most promising quasi-2D HPs suitable for PV applications.

Figure 1c–g exhibits the initial top-emitting photoluminescence (PL) spectra of the quasi-2D HP films as a function of 3D $CsPbI_3$ composition ratios with different 2D HP endmembers, clearly visualizing the differences in phase emergence behaviors along the combinatorial libraries (the photographs of the corresponding film arrays and the entire datasets of time-evolved PL spectra for each combinatorial library are shown in Figures S2–S7, and Supporting Information, respectively). In

contrast to 100% 3D $CsPbI_3$ film, where the non-perovskite yellow phase dominantly emerges, the incorporation of 2D HP end-member manifests the growths of 2D or 3D-like HP phases involving the corresponding PL spectra. For all cases, in addition to the $n = 1$ 2D phase that exclusively formed at 0% – evidenced by the single PL peak centered at ≈510–520 nm, PL spectra of the higher-n 2D phases emerge with increasing the 3D $CsPbI_3$ composition ratios. However, the trends in phase emergence behaviors show distinctive features depending on the selection of spacer cation.

We first explore the phase emergence behavior of the BA-based quasi-2D HPs – an RP-type spacer with a short alkyl chain (Figure 1c). At low 3D ratios (<10%), in addition to the dominant emergence of low-n 2D HPs (e.g., $n = 1$–3; PL peaks < 600 nm), considerable PL signals ranging 600–700 nm associated with high-n phases (e.g., $n \geq 4$) are observed, though their synthesizability are comparatively unfavorable in thermodynamics than that of the low-n counterparts.[10,11] Presumably, these high-n HPs are kinetic products, given the low molecular weight of BA and the lower emergences of such phases in other combinatorial libraries with ThEA and PEA spacers at this compositional range (vide infra); it is likely due to the higher diffusivity of BA in the precursor system and lower degree of inter-molecular interaction than other spacer cations. Note that, further increases in the 3D ratio (up to ≈25%) counterintuitively suppress the crystallization of the high-n HPs that require 3D HP building blocks, again corroborating that the emergence of these phases is thermodynamically unfavorable in such a compositional range.

With increasing 3D ratio from 25 to 35%, a progressive emergence of higher-n HPs is observed, and over ≈35%, a distinct phase consisting of 3D-like phases (centered at ≈700 nm), involving marginal $n = 1$ and 2 2D HPs, is observed. Such phase emergence features are consistently observed up to ≈90% 3D ratio. These observations indicate that, in this composition range, the BA-based 3D-like HP structures can be synthesized at a low annealing temperature (95 °C). We see inappreciable emission intensity for the compositions with over 90% 3D ratio, suggesting that thermodynamically favored non-perovskite δ-$CsPbI_3$ crystallites, rather than 3D-like HPs, are formed. This also implies that sufficient amounts of spacer cation are vital for overcoming the thermodynamics in making 3D-like HP crystallites at such a low annealing temperature.

Note that, after 10 h, the PL peak intensities of the $n = 1$ and 2 2D HPs are increased at the expense of those from the 3D-like phases across the compositional space (Figure S8a, Supporting Information). The decreased PL intensity of the 3D-like HPs indicates the temporal degradation of the corresponding crystallites upon ambient exposure during the measurements. The degradation action disintegrates the 3D-like HPs into fragmented building blocks, which are, in turn, merged into $n = 1$ and 2 2D phases. That is, BA offers insufficient ambient stability of the 3D-like HPs, which makes them impractical for PV applications. Essentially, these changes are associated with degradation action of the quasi-2D HPs, and thus, it is legitimate to assume that such spectral features showing across the quasi-2D HP compositional space are indicative of the functionality of the spacer cation on the stability of the film matrices; the appreciable spectral changes in the compositional space indicates that the corresponding spacer cation cannot benefit the stability of the quasi-2D HP films.

In contrast, DJ-spacer, BDA, exhibit different phase emergence behaviors. It is found that multiple 2D HP phases with $n \geq 3$ thicknesses emerge in the film matrix at the low 3D ratios, which separate from the $n = 1$ 2D HP (Figure 1d). These 2D HPs (e.g., $n \geq 3$) render a broad PL band ranging in 550–700 nm wavelength. The broadband PL becomes narrower with increasing the 3D ratio up to ≈35%, which then gradually converges as a strong PL band ranging in 600–700 nm wavelength. Such trends were consistent with further increasing the 3D ratio up to 90%. Note that, in the overall compositional range, the peak position of the broadband PL peak constantly locates at the lower wavelengths than that of α-$CsPbI_3$ (centered at ≈700–710 nm) or 3D-like HP seen in the BA counterpart. This suggests that, comparatively, the high-n HP phases constructed in a BDA-based quasi-2D HP system are thinner than those in the system with RP spacers. We also note that the intensity of the broadband PL is even stronger than those of $n = 1$ and 2 2D HPs. That is, BDA tends to manifest higher-n phases rather than intermediate 2D phases (e.g., $n = 2$–4 2D HPs), allowing efficient charge transport through the non-confined HP lattices[34] – beneficial to PV applications. However, distinct emergences of lower-n 2D HPs are observed across the compositional space after 10 hours (Figure S8b, Supporting Information), suggesting that BDA cannot bestow sufficient phase stability to the quasi-2D HP lattices.

The phase emergence behaviors in the aromatic RP spacers are also explored. ThEA and PEA exhibit similar phase emergence behaviors across compositional space, likely due to their similarity in molecular structure (Figure 1e,f, respectively). At low 3D ratios up to ≈10%, $n = 1$ and 2 2D HPs dominantly emerge in both systems. Meanwhile, weak PL signals associated with higher-n phases ($n \geq 3$) are also observed in the synthesized films. Comparatively, the PL emergences of these higher-n phases in both quasi-2D HP systems are weaker than those in the BA counterpart. Such discrepancy in the emergence of higher-n phases can be synergistically attributed to the heavier molecular weights of ThEA and PEA compared with BA, as well as the stronger inter-molecular interaction between the spacer cations through the aromatic rings in these molecules. The non-trivial π–π stacking behavior, together with their larger molar masses than that of BA, likely impedes the diffusion action in the precursor solution, thus restricting the formation of the kinetic products. Note that the emergence of high-n 2D HPs is more suppressed in the PEA-based system compared to the ThEA counterpart, despite the relatively lighter molecular weight of PEA. This suggests that inter-molecular interaction – particularly, the π–π stacking behavior – of PEA is stronger than that of ThEA.

In both systems, with further increasing the 3D ratios up to ≈20%, much higher-n phases progressively emerge, and then the 3D-like HP phases become dominant when the 3D ratio exceeds ≈30% (≈25% for PEA), involving marginal amounts of low-n 2D HPs. Similar phase emergence behaviors are also observed in the BA-based system, which, however, starts at relatively higher 3D composition ratios of ≈40%. This can also be explained by the retarded diffusion of the ThEA and PEA spacers. This subsequently slows down their surface coordination to the HP lattice, and such slower crystallization kinetics offers longer times for the growth of inorganic lattices, thus manifesting thicker HPs. Similar crystallization mechanisms have been proposed for the quasi-2D HPs incorporating coordinative molecular additives in

the precursor system (e.g., crown ethers, and so on), where their strong coordination actions to the inorganic lattice prevent the complete formation of 2D HPs.[35–38]

Over the 3D ratio of ≈60%, the intermediate-n (e.g., n = 3–5), as well as the n = 1 2D phase start to emerge, at the expense of the 3D-like HPs. This suggests that the formation of 3D-like HP phases is no longer favorable over this composition ratio. Essentially, this seems to be counterintuitive to the conventional perovskite chemistry, where, stoichiometrically, higher-n HP phases are deemed to emerge when the 3D composition ratio becomes dominant in the system. In fact, analogous phase emergence features were observed in formamidinium (FA)-based quasi-2D HPs,[14] hypothesizing that thermodynamically favorable δ-$FAPbI_3$ phase can disturb the growth of 3D-like phases at such high 3D composition ratios. Considering this, the observed scenarios in this study can also be associated with the formation of a thermodynamically favorable δ-$CsPbI_3$ phase.

Temporal stability of the quasi-2D HP phases in ThEA- and PEA-based systems, after exposing the films for 10 h in an ambient atmosphere, are also assessed (Figure S8c,d, Supporting Information). Appreciable intermediate-n 2D HPs emerge in the ThEA-based quasi-2D HP composition space, at the expense of the 3D-like phase. In contrast, marginal changes in phase emergence behaviors are observed across the compositional space of the PEA-based system. These observations imply that PEA cation offers better phase stability compared to ThEA. It is known that PEA in quasi-2D HPs enhances phase stability, as the phenyl ring can protect the inorganic lattice against external stimuli such as O_2 and H_2O.[12,30] Considering this, the poor stability of ThEA-based quasi-2D HP is likely associated with the heterocyclic structure of thiophene; this can offer a different scenario in chemical interactions that cannot benefit the stability of the HP lattice.

Next, we examined the effect of a larger bulky spacer having two phenyl rings. DPA renders completely different phase emergence features in quasi-2D HPs compared with other systems (Figure 1g). It should be noted that pure DPA_2PbI_4 cannot be crystallized unless a minute concentration of 3D $CsPbI_3$ (at least 2 mol.%) is incorporated in the precursor state. With a small amount of 3D precursors, crystallization occurs, producing yellow-colored films exhibiting distinctive asymmetric PL spectra peaked at ≈490 nm. Such an unconventional HP crystallization feature and PL behaviors are likely due to the steric hindrance of DPA caused by the proximity of the neighboring phenyl rings at the 2D HP surface.[28]

Similar to other RP-type systems, the progressive emergences of intermediate-to-high-n phases are also observed in DPA-based quasi-2D HP compositional space, where such features are manifested at even lower 3D ratios – from ≈10% to 25% – than the PEA counterparts. The heavier molecular weight of DPA than ThEA or PEA further slows down the diffusion of the spacer in the solution, which thereby attributes to the results. From the 3D ratio of 30 to 90%, the 3D-like phases become dominant, which also involves considerable n = 1 2D phase. Note that, after 10 hours under ambient conditions, though the PL intensity of the intermediate-n phases is slightly enhanced at the low 3D ratios (<20%), overall, no appreciable changes in the spectral features across the compositional space are observed (Figure S8e, Supporting Information). This indicates that the DPA spacer manifests excellent stability of the HP lattices, as the two phenyl rings in the molecule can effectively shield the HP lattices from the oxidative species.[16,30]

Having explored the phase emergence behaviors at the top surfaces, we assess the phase emergence behaviors at the bottom-surface to investigate the vertical phase homogeneities in each quasi-2D HP combinatorial library (Figure S9, Supporting Information) – a key factor determining optoelectronic functionalities. For RP-type HP systems, it is known that, in contrast to the top surfaces where 3D-like phases are abundant, the low-n (e.g., n = 1 and 2) 2D phases are dominant at the bottom of the matrices (Figure S9a,c–e, Supporting Information). This is likely due to the imbalanced crystallization kinetics of each HP phase, where the crystallization of the 3D-like HP phase majorly takes place at the solution–air interface initially.[31,32] The precursor ions of (quasi-)2D HPs reside longer time in the solution and are concentrated at the bottom surface, rather than crystallizing at the top surface – attributed to the stronger solvent–solute interactions due to the larger polarity of the spacer cations,[13,39] which thereby undergo crystallization. Such distinct phase inhomogeneity along the vertical direction can hamper appropriate charge transport, thus significantly restricting PV performance. In contrast, for Cs-BDA quasi-2D HPs – a representative DJ-type HP system in this study, similar phase emergence behaviors are observed at both the top and bottom surfaces (Figure S9b, Supporting Information). This suggests that more homogenized phase distributions are manifested along the vertical direction of the DJ-based quasi-2d HP film matrices, rendering a smoother energetic landscape that allows more efficient vertical charge transport in PV applications. Note that such a difference also implies that the crystallization mechanism of DJ-based quasi-2d HPs does not follow that of RP-type counterparts.

Summarizing, for all quasi-2D HP systems, high-n phases emerge with increasing 3D composition ratios. For RP-type systems, higher-n or 3D-like phases emerge at the top surface when the heavier spacer cation is employed, which simultaneously suppresses the growth of low-n 2D HP kinetic products (e.g., n = 2–4). In contrast, n = 1 and/or 2 2D HPs are dominant at the bottom of the film matrices. DJ-type spacer BDA homogenizes the 2D phases along the vertical direction. However, it also manifests thinner 3D-like phases with broader thickness distributions, offering a larger bandgap with energetic inhomogeneities that impede efficient charge transport upon PV applications.

To better understand the global trends in the spacer-dependent phase emergence behaviors across compositional space, we utilize non-negative matrix factorization (NMF), an unsupervised ML approach. This multivariate data analysis has been successfully implemented to explore the large chemical space in the quasi-2D HPs, which effectively identifies key features associated with complex materials systems.[13,14,27] Through NMF deconvolutions, time-evolutions of key PL features – reflecting the corresponding HP phases – and their composition dependencies (both at the top and bottom surfaces) are identified. This allows us to visualize the qualitative phase diagrams in each combinatorial library. **Figures 2** and S10 (Supporting Information) reveal the key phase emergence behaviors at the top surface of each combinatorial library. Here, we used three components (four for the

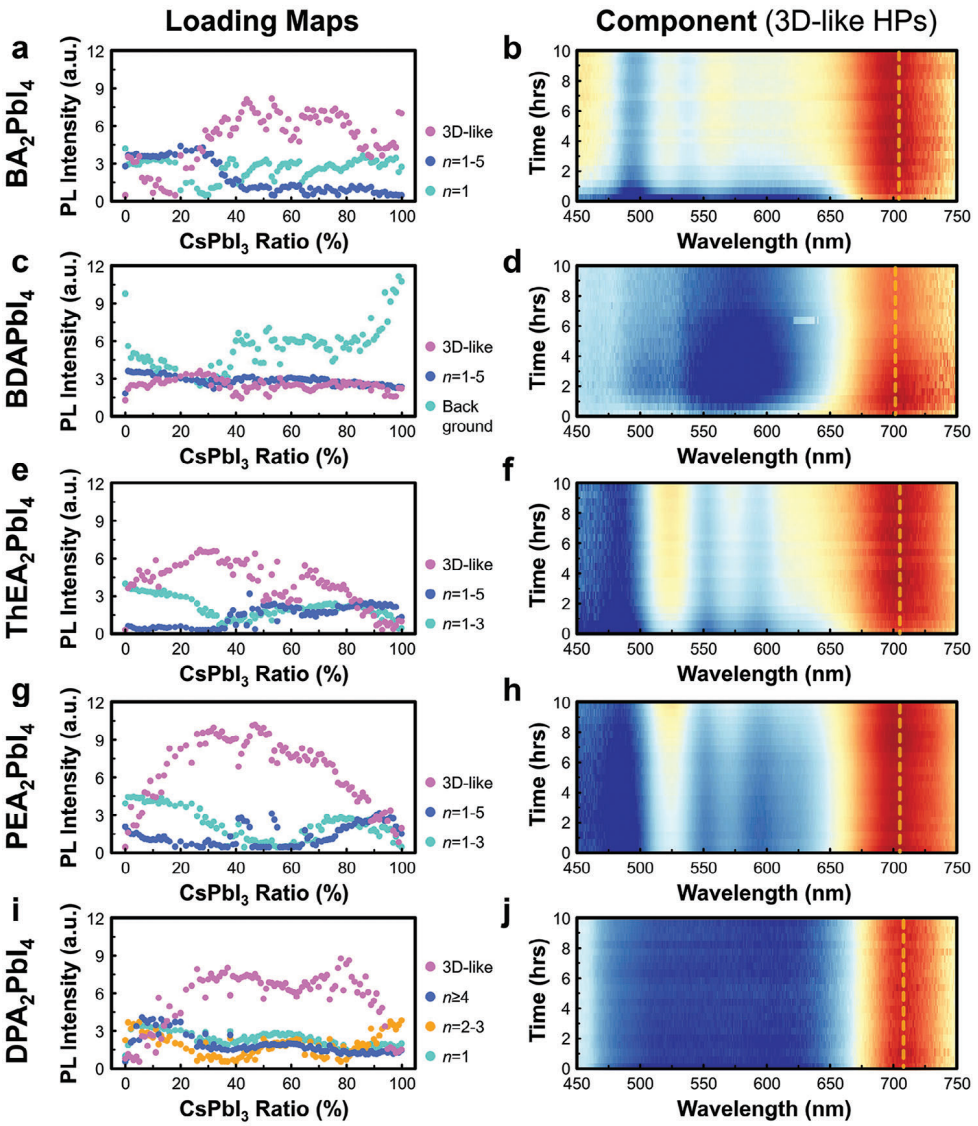

Figure 2. NMF-deconvoluted a,c,e,g,i) loading maps and b,d,f,h,j) PL components corresponding to 3D-like HP phases, from the top-emitting PL spectra for the combinatorial libraries of quasi-2D HP films with different spacer cations: a,b) BA, c,d) BDA, e,f) ThEA, g,h) PEA, and i,j) DPA, respectively.

DPA-based system) as an optimal number for NMF analysis, which can reasonably deconvolute the PL datasets.

Through NMF, we first examine the phase emergence behaviors in the BA-based quasi-2D HP system, having a short aliphatic chain and light molecular weight. At the top surface, it is found that low-n 2D HPs – particularly, $n = 1$ – emerge across the whole compositional range (Component 2; Figure 2a; Figure S10a, Supporting Information). Additionally, a very weak PL peak centered at ≈710 nm emerges– assigned to be α-$CsPbI_3$ having a red-shifted PL from the that of the 3D-like HPs, which quickly disappears within an hour (Figure S9a, Supporting Information). This indicates that the α-$CsPbI_3$ HP phase, with a cubic lattice structure, initially forms at the low annealing temperature, which then quickly disintegrates or transforms to other phases due to its intrinsic thermodynamic instability. Note that such a feature cannot be recognized by manual exploration of the PL spectra (Figures S3–S7, Supporting Information), showing the effectiveness of the NMF technique on studying such large datasets. Also, multiple low-n HPs (e.g., $n = 1$–5) prominently emerge up to 30% of $CsPbI_3$, which are then suppressed at the higher composition ratios (Component 3 in Figure S10a, Supporting Information) – as seen in the corresponding PL spectra as a function of 3D ratios Figure 1c. Meanwhile, the PL of the 3D-like phases – centered at ≈700 nm – starts to emerge for 3D ratios over 40% (Figure 2b), suggesting that 3D-like phases start to develop. In contrast, for the case of BDA, with an additional ammonium head in the structure of the spacer molecule, multiple low-n HP phases ($n = 1$–5), as well as the 3D-like phases emerge across the entire compositional range (Figure 2c,d; Figure S10b, Supporting Information). It is found that the PL intensity of the latter phases gradually decreases over time, attributed to their poor stability. Note that the spectral signature of the emergence of α-$CsPbI_3$ HP is not observed in this system, implying that BDA cannot manifest the construction of the cubic HP lattice.

NMF-deconvolution reveals the similarity in global phase emergence behaviors between ThEA- and PEA-based quasi-2D HP systems (Figure 2e–h; Figure S10c,d, Supporting Information). Qualitatively, the deconvoluted PL features are also analogous to those in the BA-based system, rather than the BDA counterpart, indicating that the type of the spacer cations primarily determines the overall phase emergence behaviors. In both cases, at the top surface, $n = 1$ and other low-n 2D HPs emerge at low-3D composition ratios, which are gradually suppressed up to the 3D ratio of 40% (Component 2 in Figure S10c,d, Supporting Information, respectively). Above 40% and 60% for the ThEA- and PEA-based systems, respectively, these phases start to emerge again and then disappear over 90% 3D ratio. In both cases, NMF deconvolution captures the transient emergence of the α-$CsPbI_3$ HP (Component 3), which survives longer times than that observed in the BA counterpart. This implies that the aromatic rings can provide better stability to the HP lattices.

It is worth noting that, particularly for the PEA-based system, there is a specific 3D composition range of 40–60%, where the emergence of 3D-like phases becomes dominant while the other phases are greatly suppressed or are at the nominal level (Figure 2g,h). A similar trend was observed in the PEA-formamidinium (FA) quasi-2D HP systems; it was confirmed that vertically aligned 3D-like phases exclusively emerge at this compositional range, expected to benefit PV performances.[14]

For DPA-based quasi-2D HPs (Figure 2i; Figure S10e, Supporting Information), n = 1–5 2D phases (components 2–4 in Figure S10e, Supporting Information) concurrently emerge with a similar trend across the entire compositional range, particularly prominent at low 3D concentrations (<30%). The stable 3D-like HPs emerge at a large compositional range of 20–85%. These observations imply that the formation of low-n 2D phases is much more restricted than those in ThEA and PEA-based counterparts. Note that the PL peak of the 3D-like HPs exhibits an almost identical PL center to that of α-$CsPbI_3$ HP (Component 2), suggesting that the 3D-like phase in DPA-based quasi-2D HP has thick inorganic lattices in the HP lattices (i.e., very high n values) on par with those in bulk 3D $CsPbI_3$ HPs.[40] Presumably, the incomplete surface coverage of DPA, as a result of steric hindrance,[28] provides appropriate strain to the inorganic lattice to manifest the cubic α-$CsPbI_3$ HP phase, which cannot be achieved by using the conventional spacer cations.

The observed correlations between the phase emergence behaviors and the selection of spacers collectively infer distinctive principles for designing quasi-2D HP matrices. In general, heavy molecular spacers manifest the growth of high-n or 3D-like HP phases, which are also more stable than the pure 3D $CsPbI_3$ counterpart and therefore benefit PV applications. However, at the same time, this simultaneously causes the strong emergence of low-n (particularly, $n = 1$) 2D HPs at the bottom, which act as an energetic barrier for charge transport. The DJ-type spacer can greatly mitigate such vertical phase inhomogeneity, although this adversely compromises the phase stability. While the spacers having aromatic rings offer better stability to the 3D-like phases compared to the aliphatic chain, practically, the phenyl ring is more advantageous to phase stability than other heterocyclic rings.

By using NMF analysis, the phase emergence behaviors at the bottom surface of the films are also examined (Figure S11, Supporting Information). As observed from composition-dependent PL spectra (Figure S9, Supporting Information), the RP-type quasi-2D HP systems exhibit the dominance of the low-n ($n = 1$ and 2) 2D phases across the entire compositional range. These 2D HPs have larger bandgaps than those of 3D-like counterparts, manifesting energetic barriers between the underlying charge transport layer and the 3D-like HP photoactive layer. Such an energetic landscape, in turn, can impede efficient charge transport across the vertical direction, and consequently, curtail PV performances. Indeed, those quasi-2D HP films exhibit low PV performances (Figure S12, Supporting Information, detailed device fabrication and characterizations in Experimental Section); here, an optimal 3D composition ratio of 60%, where the exclusive emergence of 3D-like phases is expected to be most probable, was employed. These observations suggest that mitigation of vertical phase inhomogeneities in the quasi-2D HPs is vital for demonstrating efficient PV devices.

Note that NMF analysis also identifies similar phase emergence behaviors at both the top and bottom surface of the BDA-based quasi-2D HPs (Figure 2b; Figures S10b,S11, Supporting Information), again revealing the vertically homogenized phase distributions in this system. While this feature can benefit the optoelectronic performances when the films are employed in PV devices, however, an extremely low power conversion efficiency (PCE) of 0.39% is recorded (Figure S12, Supporting Information). Such poor PV performance is likely attributed to considerable charge carrier loss through the abundant surface defects as well as the emergence of non-HP δ-$CsPbI_3$ crystallites in the quasi-2D HP matrices (vide infra).

2.2. Local Phase Inhomogeneities and Chemical Interactions in the Quasi-2D HPs

Exploration of the global phase emergence behaviors in the quasi-2D HP systems reveals that various HP crystallites emerge, thus causing notable phase inhomogeneities in the film matrices. To spatially resolve and investigate the local phase inhomogeneities in the synthesized film matrices, Hyperspectral cathodoluminescence (CL) microscopy, integrated with a Scanning electron microscope (SEM), is utilized. **Figure 3a** shows the surface SEM images of the quasi-2D HP films with different spacer cations. Here, a fixed 3D ratio of 60% was adopted for constructing quasi-2D HP films, which most likely offer 3D-like matrices as deduced from NMF analysis. It was found that the selection of a molecular spacer renders a distinctive surface morphology.

The BA-based film exhibits a rough and crumbled surface morphology with many voids (diameters of 100–300 nm), suggesting that considerable defects are likely present in the matrix. Particularly, the voids can be attributed to the low boiling point of BA (78 °C), which can facilitate its vaporization upon film fabrication. In the BDA-based film, rod-shaped structures emerge. It is found that these features are exactly overlapped with the emission signals in the corresponding 445 nm-filtered CL map, which is confirmed as δ-$CsPbI_3$ (Figure 3b).[41,42] Note that appreciable 445-nm signals are also observed in BA-based quasi-2D HP film, although the corresponding crystallites are not found in the SEM image. This suggests that the δ-$CsPbI_3$ crystallites are intercalated within the HP matrices, as a result of the deformation from the 3D-like phases.[41–43] In contrast, the rod-shaped

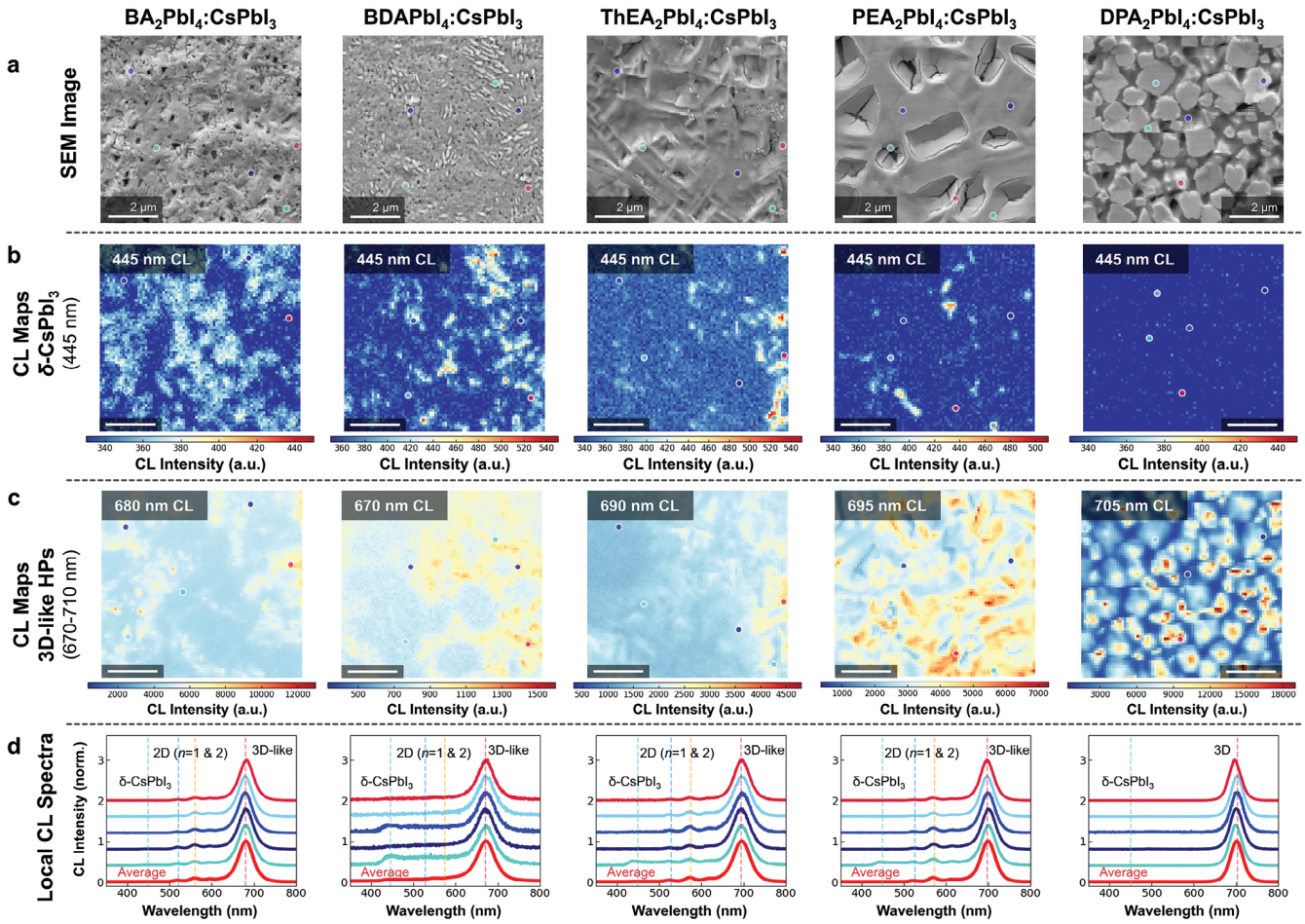

Figure 3. Hyperspectral cathodoluminescence (CL) microscopy characterizations. a) SEM images and the corresponding b) 445- and c) 670–710 nm-filtered CL intensity maps of the quasi-2D HP films with different spacer cations. d) Local CL spectra collected at the 5 different spots (marked with colored circles in the SEM images and the CL maps) in each film. For each case, an average CL spectrum (across the scanned area) is also included (red curve).

δ-$CsPbI_3$ crystallites at the BDA-HP film surface corroborate that both HP and non-HP phases are concurrently constructed upon the crystallization process, rather than deformation.[42,43] We hypothesize that the slow crystallization dynamics in this system, attributed to the strong chemical interaction between BDA and inorganic precursors, causes the separated growth of quasi-2D HPs and non-HP phases, rather than promoting the higher-n HP growths (vide infra).

Also, a large number of voids (smaller than the BA counterpart; <100 nm) are observed. Given the high boiling point of BDA (≈158 °C), those voids can be attributed to both slower crystallization kinetics of DJ-type 2D HPs and the thermodynamic preference of the δ-$CsPbI_3$ formation at the low processing temperature.[44,45] We map the CL signals at ≈680–700 nm for each film (Figure 3c). These wavelengths respectively correspond to the CL peak of the 3D-like HPs (the average and local CL spectra collected from each film are shown in Figure 3d). In both cases, stronger CL signals of 3D-like phases are observed in the surface voids. Similar CL intensity enhancement is observed from the grain boundaries in 3D HP films, attributed to the higher free carrier concentrations promoting radiative recombination.[42,46] Given such voids are associated with the evaporation of the spacer, it is hypothesized that large amounts of molecular spacers are congregated at the local sites. In turn, this can manifest a higher density of the coordinated spacers on the HP surface, thereby passivating the surface defects and accelerating radiative recombination.[47] Note that the CL peak of the 3D-like phase in BDA-based film appears at ≈670 nm, which is blueshifted as compared to the CL peak observed in the other systems. This aligns well with the blueshifted absorption edge of BDA-based film (Figure S13a, Supporting Information), suggesting that BDA indeed forms thinner 3D-like HP phases with a larger bandgap, as also evidenced from the blueshifted PL peaks (Figure 1d; vide supra).

ThEA- and PEA-based quasi-2D HPs exhibit softer surface morphologies than BA and BDA counterparts. ThEA-based film exhibits angulated surface textures, likely attributed to the formation of small-n 2D HP phases. Also, rectangular particles exhibiting 445 nm CL are intercalated to the film surface (Figure 3a,b), indicating that δ-$CsPbI_3$ also emerges in this system. Note that the area exhibiting the local δ-$CsPbI_3$ signals is smaller than that in the BA-based system. These suggest that ThEA offers better

stability of the 3D-like phases than BA, though it is still insufficient to realize PV-grade films. The PEA-based film renders a flat and smooth surface morphology, though some of the areas exhibit collapsed features. Note that the local spots emitting δ-$CsPbI_3$ are notably reduced and there was no appreciable structural feature correlating with the emission spots (Figure 3c). This indicates that PEA offers much more improved phase stability of quasi-2D HPs than ThEA, thereby suppressing phase deformation. Meanwhile, stronger CL intensities of 3D-like HPs are observed along the cracked boundaries in the films. Such a distinct local contrast in 3D-like HP CL indicates that substantial chemical inhomogeneities are manifested in the film surface, which can disturb the energetic landscape and thereby hamper efficient charge transport.

Flat and island-like features are distinctively observed in the DPA-based quasi-2D HP films (Figure 3a). Interestingly, no appreciable CL signal associated with δ-$CsPbI_3$ is observed (Figure 3b), attributed to the outstanding phase stabilizing effect of DPA. The 3D-like HP phases exhibit CL peaked at the longer wavelength of 705 nm (Figure 3c) than that of the others, which almost replicates the emission of bulk $CsPbI_3$.[40] This indicates DPA manifests the formation of thicker 3D-like HPs at the top surface. The steric hindrance between the neighboring DPA phenyl rings can restrict the complete surface coverage of the spacers on the HP lattice. This scenario can impede the termination of crystallization as 2D HP phases, thereby promoting the formation of thicker HP lattices. Note that some immature crystallites, without offering flat and island-like structures, are observed. Local CL spectra reveal that these structures exhibit blueshifted CL (≈10 nm) peaks (Crimson-colored curve, Figure 3d), indicating the formation of quasi-2D HPs thinner than those at the foremost top surface. This suggests that DPA cations are more abundant along the depth of the film, which can make more dimension-confined HP lattices.

Overall, among these molecular spacers, it is anticipated that PEA-based quasi-2D film is the most suitable photoactive matrix. Despite notable chemical inhomogeneity, it can offer a stable and smooth film surface while minimizing the local phase inhomogeneity, which benefits PV performance and stability. These features align with the estimated trend of band-tail energy derived from the absorption spectra of the corresponding films, represented by Urbach tail energy (E_u), as shown in Figure S13b (Supporting Information). For instance, the significant presence of defective phases in the BDA system results in the highest E_u of 62.8 meV, indicating a disordered energy landscape. In contrast, the smallest E_u of the PEA-based system (excluding the case of DPA) confirms that minimizing local phase inhomogeneities effectively suppresses energetic inhomogeneities of the entire matrix thereby, promoting better charge transport. The smallest E_u of DPA-based quasi-2D film is likely due to the development of dominant 3D α-$CsPbI_3$ HP crystallites in the matrix as revealed by hyperspectral CL analysis (Figure 3), despite the film's substantial structural inhomogeneity. This suggests that the calculated E_u reflects the energetic inhomogeneities of the entire matrix caused by phase formation, rather than the structural inhomogeneity, which is more related to interfacial energetics in multilayered devices. In contrast, such an imperfect surface coverage of the crystallites in the DPA-based quasi-2D HP film is not expected to offer good charge transport features and PV performances, though the DPA indeed bestows excellent stability of the photoactive 3D-like phases.

To gain insights into the crystallographic information, we collected grazing-incidence wide-angle X-ray scattering (GIWAXS) patterns of the quasi-2D HP films (Figure S14a–c, Supporting Information). We apply three different incidence angles, 0.1°, 0.2°, and 0.5°, where the small and large angles majorly reflect the crystallographic information of the foremost surface and the bulk interior of the films, respectively. This allows us to explore the progressive change in phase emergence behaviors along the vertical directions.

The BA-based film exhibits strong Bragg spots aligned along the Q_z = ≈1.0 and ≈2.0 $Å^{-1}$. This is a representative signature for the vertically aligned 3D HP lattice, which has been observed from various quasi-2D HP systems.[14] That is, BA promotes the growth of vertically aligned 3D-like HP phases. Figure S15a (Supporting Information) shows the corresponding 1D scattering profiles of the BA-based quasi-2D HP film along the out-of-plane (OOP) and in-plane (IP) directions, respectively. In addition to the 3D $CsPbI_3$ lattice, scattering modes of n = 1 and 2 2D HPs are observed. These peaks become stronger with increasing the angle of the X-ray beam, particularly along the OOP direction, indicating that these face-on stacked 2D HP phases become dominant toward the bottom surface. Meanwhile, appreciable peaks of δ-$CsPbI_3$ and PbI_2 are observed. These phases are produced as a result of the deformation of quasi-2D HP,[41–43] indicating its poor stability in agreement with the emission behavior.

Distinctive Debye–Scherrer rings are observed in the 2D GIWAXS pattern of the BDA-based film, suggesting the crystallites in the matrix majorly exhibit random orientation (Figure S15b, Supporting Information). In the corresponding 1D profiles, strong scattering peaks of δ-$CsPbI_3$ and PbI_2 crystallites are observed, indicating the predominance of these phases. Note that these peaks are relatively stronger than the 3D $CsPbI_3$ peak at the lower incidence angles, suggesting these degradation products are located around the top of the film surface.

The 2D GIWAXS patterns of the ThEA-based film majorly exhibit ring-shaped patterns, whereas the peaks of the principal 2D HPs (e.g., n = 1 and 2 phases) are strong along the OOP direction (Figure S15c, Supporting Information). These 2D HPs become predominant at the bottom, which agrees well with the vertical phase inhomogeneity seen in PL observations. Meanwhile, the emergence of weak Braggs spots along the Q_z = ≈1.0 $Å^{-1}$ indicates that the 3D-like HP phases in this system are also vertically aligned. Moreover, strong emergences of δ-$CsPbI_3$ and PbI_2 crystallites corroborate that ThEA cannot bestow good phase stability of the resulting quasi-2D HPs. In the PEA-based film, the Braggs spots become more discrete, whereas the scattering rings are weakened (Figure S15d, Supporting Information), suggesting more oriented growth of the crystallites in the matrix. According to the 1D scattering patterns, overall, similar phase emergence and vertical phase inhomogeneities are observed in the PEA-based system. A stark difference from ThEA counterpart is the absence of the δ-$CsPbI_3$ and PbI_2 crystallites. This further corroborates that PEA indeed offers good stability in the quasi-2D HP thin films.

The DPA-based HPs exhibit random-oriented crystallographic features, as confirmed by the ring-shaped scattering patterns (Figure S15e, Supporting Information). Similar to the PEA-based

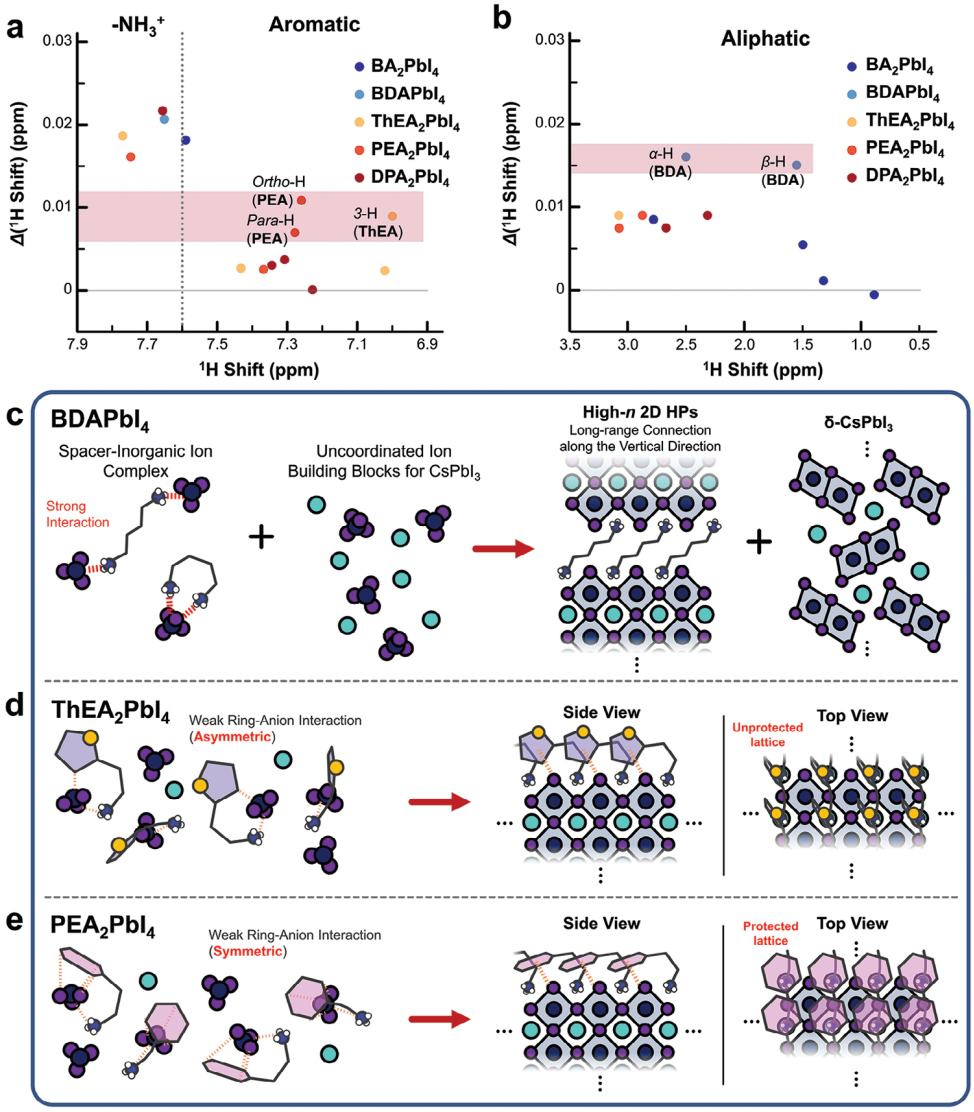

Figure 4. Estimated magnitudes of proton downshifts, Δ(^{1}H Shift), of the protons in the a) ammonium and aromatic group, and b) alkyl chains for the corresponding spacer cations in the precursor solutions, derived from the solution-phase ^{1}H nuclear magnetic resonance (NMR) spectra. Schematics describing the chemical interaction and the molecular geometry between the spacer cation and the inorganic building blocks for c) BDA, d) ThEA, and e) PEA-based quasi-2D HP systems, respectively.

system, there was no appreciable signal from the δ-$CsPbI_3$ and PbI_2 crystallites in the DPA-based quasi-2D HPs. Although this indicates that DPA can provide stable 3D-like HP lattices, such random-oriented crystallites, together with the distinctive abundance of $n = 1$ and 2 2D HPs, infer inefficient charge transport environments that are likely detrimental to PV applications.

To gain an understanding of the chemical interaction between the molecular spacers and precursors, which can affect the crystallographic structures and phase distributions in the films, proton nuclear magnetic resonance (^{1}H-NMR) spectroscopy is conducted on the corresponding precursor solutions. Figures S16 and S17 (Supporting Information) exhibit ^{1}H-NMR spectra of the precursor solutions, together with the corresponding solution after dissolving spacer cation-iodide salts, allowing us to identify the chemical changes by the interaction with the inorganic ions.

For all cases, the $-NH_3^+$ peak undergoes notable downfield shifts (≈0.02 ppm) when the inorganic precursors are incorporated, indicating the strong chemical interaction between the ammonium group and the inorganic precursors (**Figure** 4a). In addition, for BA, the characteristic peaks of hydrogens at α-carbons also exhibit appreciable downfield shifts in the precursor solution (Figure 4b; Figure S16a, Supporting Information), indicating that partial electron transfer from BA to the inorganic precursors occurs. Note that the progressive weakening of the ^{1}H downfield shifts is observed from β- to δ-protons position where the latter does not exhibit appreciable peak shift. This suggests that the electrostatic interaction mainly takes place in the ammonium group. In BDA, the protons at both the α- and β-carbon exhibit strong and comparable downfield shifts (≈0.016 ppm) when the inorganic precursors are present (Figure 4b; Figure S16b, Supporting Information). This indicates the existence of a strong

chemical interaction between the inorganic ions and the BDA molecules – across the entire molecular structure. Presumably, two interactive sites (i.e., ammonium groups) in BDA manifest tight coordination with the HP building blocks in the solution phase (Figure 4c). Such strong chemical interaction between spacer and inorganic building blocks not only offers slow crystallization kinetics but also maintains ionic coordination during the entire film fabrication process – starting from liquid–air (top) to the liquid-substrate (bottom) interfaces. This likely mitigates the vertical phase inhomogeneity of the quasi-2D HP matrix. However, as the spacer–precursor interaction is too strong, some of the 3D $CsPbI_3$ precursors cannot be involved in the crystallization of quasi-2D HP lattice. Subsequently, a separate crystallization of these 3D precursors takes place, which likely forms δ-$CsPbI_3$ that are intercalated into the film matrix, due to the thermodynamic incompatibility of the α-HP phase at such a low annealing temperature.

In both ThEA and PEA, the protons at $-NH_3^+$ and the alkyl bridge exhibit sequential downfield shifts as seen in the BA system (Figure S16c,d, Supporting Information), suggesting the spacers primarily interact with the inorganic ions through the ammonium head. In contrast, only the proton at the 3-carbon in ThEA (marked with a yellow circle) exhibits appreciable downfield shifts (Figure S17a, Supporting Information), whereas the protons at ortho- and para-positions of PEA undergo such downfield shifts (Figure 4a; Figure S17b, Supporting Information). This suggests that the respective chemical interaction between the spacer and precursor ions manifests different molecular geometry of ThEA and PEA in the solutions. Specifically, ThEA renders an asymmetric molecular geometry, where both the ammonium head and 3-carbon in the thiophene ring interact with the inorganic ions (Figure 4d). In contrast, PEA can offer symmetric molecular geometry that the phenyl ring faces on the inorganic ions (Figure 4d). This asymmetric chemical interaction between ThEA and inorganic ions is further evidenced by comparing the corresponding ^{1}H-NMR spectra collected at a higher temperature (e.g., 80 °C), as shown in Figure S18 (Supporting Information). A significant difference in the magnitude of upfield shift for the hydrogens at the 3-carbon position in ThEA between the neat spacer and precursor solutions confirms a distinct asymmetric spacer–inorganic interaction, whereas the PEA exhibits a symmetric interaction. Additionally, ThEA shows larger peak upshifts of aromatic hydrogens compared to PEA at 80 °C, likely due to its weaker inter-molecular π–π stacking characteristics relative to PEA. We hypothesize that such molecular geometry can be maintained even during the crystallization process. This in turn manifests the distinctive ring alignments at the HP surfaces for each case, thus bestowing a stark difference in phase stability upon ambient exposures. The upright geometry of ThEA cannot protect the HP lattice and compromise the lattice stability (Figure 4d). In contrast, PEA's "umbrella" geometry can effectively block the environmental O_2 and H_2O, thus effectively protecting the inorganic lattice and improving the phase stability (Figure 4e) – consistent with the conclusion based on PL, CL, and GIWAXS observations. Similar symmetric molecular geometry is anticipated from the ^{1}H NMR spectra of the DPA-based system (Figures S16e,S17c, Supporting Information), which strongly agrees with our observations.

2.3. Machine Learning-Driven Exploration of Ternary Quasi-2D HP System

The high-throughput exploration and detailed chemical and structural analysis reveal the profound roles of spacer cations in making quasi-2D HPs. Among them, BDA homogenizes the vertical phase distribution while compromising phase stability, whereas PEA offers a flattened HP surface with excellent phase stability at the expense of vertical phase inhomogeneity. Considering these features, it is reasonable that employing both spacer cations to quasi-2D HPs can synergistically allow us to exploit the advantages of each component while compensating for the drawbacks.

Inspired by this hypothesis, we designed a ternary compositional space by using $BDAPbI_4$, PEA_2PbI_4, and $CsPbI_3$ as end-members, and the phase emergence behaviors of this new combinatorial library are explored via high-throughput automated experimental workflow. Figure S19a (Supporting Information) exhibits the synthesized quasi-2D HP arrays where the exact composition ratios in each film are summarized in Figure S19b (Supporting Information).[26] Similar to the binary systems, time-evolved PL spectra of the films are collected at the top and bottom surfaces, as shown in Figure S20 (Supporting Information).

To effectively identify the global phase emergence behaviors, we employ NMF deconvolution to the PL datasets with four optimal components (Figure S21, Supporting Information). Here we implemented Gaussian processing (GP) regression to compensate for the uncertainty caused by the large compositional steps (8%), which effectively interpolates between the NMF components in the loading maps.[26] In both top and bottom surfaces, the emergence maps of $n = 1$, $n = 2,3$, $n \geq 4$ 2D, and 3D-like HP phases in the ternary compositional space are visualized. We focus on the phase emergence behaviors of the 3D-like HPs (i.e., Phase Set 4 in **Figure 5**a), which shows high probabilities at the lower right corner in the ternary phase diagram – <15% $BDAPbI_4$, 15–40% PEA_2PbI_4, and 60–70% $CsPbI_3$ – for both the top and bottom surfaces. That is, the compositions within this range are anticipated to provide 3D-like HP phases while the vertical phase inhomogeneities are greatly mitigated. Specifically, we manually select three compositions – $CsPbI_3$:PEA_2PbI_4:$BDAPbI_4$ of 76:16:8, 68:24:8, and 60:32:8 – as optimal coordinates in the ternary diagram, which is likely suitable for PV applications. Indeed, the ternary quasi-2D HPs film with a 60:32:8 composition ratio exhibits a homogenized, and δ-$CsPbI_3$-free surface, as seen in hyperspectral CL characterization (Figure S22, Supporting Information), validating the effectiveness of NMF-based prediction.

To further explore the ternary compositional space and thereby realize the optimized 3D-like HP matrix for the PV applications, we employ a newly developed Gated-GPBO active learning approach to drive the exploration within the compositional space (see details in Note S1, Supporting Information). The Gated-GP approach introduces flexibility in addressing the challenges of real-world applications. Unlike multi-fidelity and multi-objective optimization methods, Gated-GP does not rely on correlations between properties. Instead, it employs a gating mechanism to dynamically refine the optimization space. In Gated-GP, the primary optimization is guided by a classical BO approach targeting a specific property within a given space. Simultaneously, a

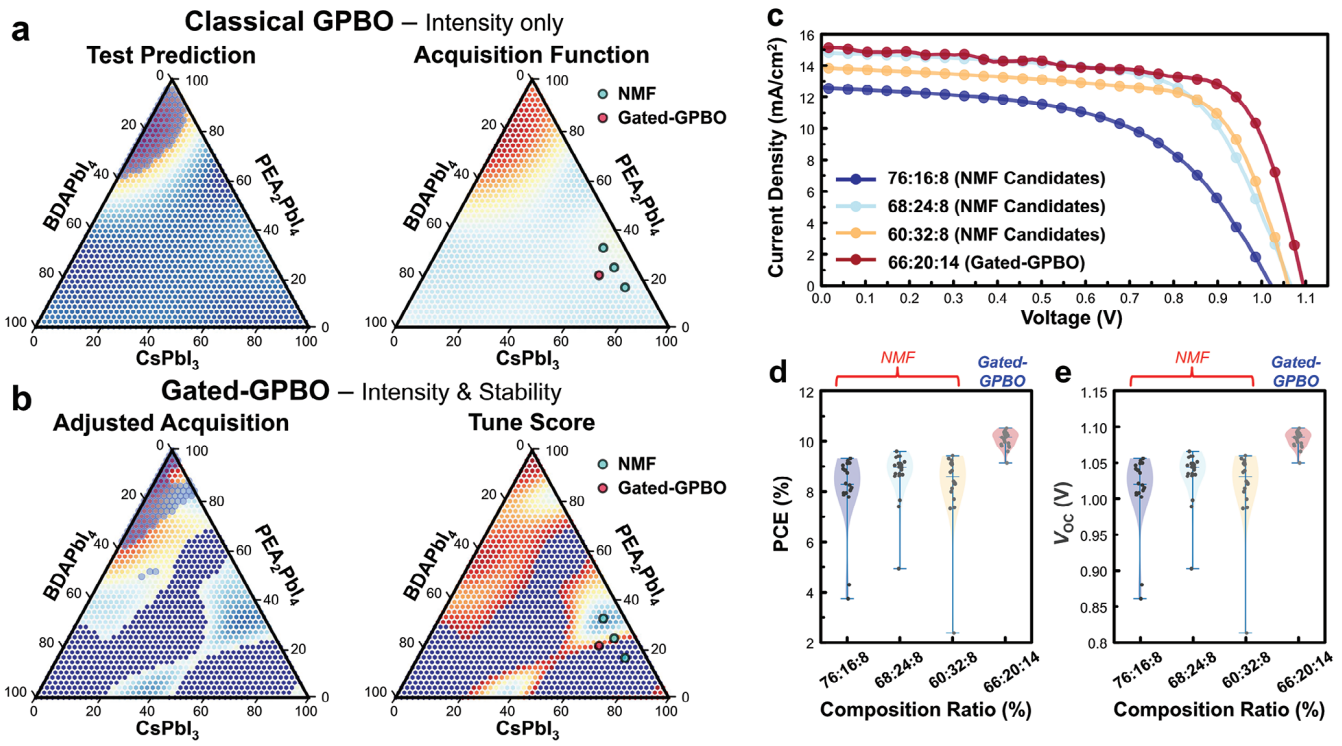

Figure 5. Ternary-compositional maps of target functionality of the quasi-2D HPs visualized by a) classical BO and b) Gated-GPBO, respectively. c) *J–V* curves of the champion PVs employing quasi-2D HPs photoactive layer designed by NMF and Gated-GPBO. d,e) Statistical plots of d) PCE and e) V_{OC} of PV devices employing quasi-2D HPs photoactive layer designed by NMF and Gated-GPBO (based on 20 individual devices).

surrogate model—a GP in this work—predicts another property and adjusts the optimization space accordingly. For example, in this study, the optimization focuses on PL intensity, representing optoelectronic properties, while a GP model predicts stability based on measured results. This approach ensures good performance for the primary property while maintaining an acceptable level for the secondary property. A key strength of Gated-GP is its flexibility in accommodating additional properties by introducing more gating mechanisms. This can be achieved with a small computational cost, making it scalable for complex optimization tasks. In addition, Gated-GP does not require strong correlations between the properties being optimized. This independence enhances its applicability across diverse scenarios.

We first implement a classical GPBO which solely takes account into the PL intensity of the films (Figure 5a). In the Gated-GPBO, an additional GP model is implemented that takes accounts into an instability score to find the compositions that render a stable PL peak that is close to the target wavelength (>600 nm). Experimentally, we conducted five iterations of drop-casting synthesis, each consisting of 96 distinct compositions, resulting in a total of 480 compositions being evaluated. After each synthesis, the experimental results, including PL measurements, were incorporated into the Gated-GPBO model. This iterative feedback loop allowed the model to refine its predictions and suggest the next set of compositions based on the data from the previous iteration (Details regarding the Gated-GPBO results of each iteration can be found in the notebook of the Gated-GPBO-driven exploration in the Experimental Section). Each synthesis cycle was completed in under two hours, enabling us to rapidly explore the compositional space and efficiently target regions of interest. This high-throughput approach not only accelerated the discovery process but also allowed for the identification of stable and optimized compositions that aligned closely with the Gated-GPBO model predictions, enhancing both the precision and effectiveness of the compositional exploration. The Gated-GPBO predicted ternary diagrams manifesting the target functionalities are shown in Figure 5b. It is found that the target functionality emerges close to the compositional space analyzed by NMF (Phase Set 4 in Figure 4a). Specifically, it visualizes a narrow channel along the ≈50% $CsPbI_3$ line profile. We refine a ternary composition 66:20:14 as a Gated-GPBO-designed composition, which is collectively shown with the NMF-predicted compositions in Figure 5.

To comparatively validate the functionality of quasi-2D HPs with designed compositions that NMF-based prediction and Gated-GPBO respectively suggested, we assess the performances of p-i-n type PVs employing these matrices as a photoactive layer; a device architecture of ITO/poly[bis(4-phenyl)(2,4,6-trimethylphenyl)amine] (PTAA)/Poly(9,9-bis(3′-(*N*,*N*-dimethyl)-*N*-ethylammoinium-propyl-2,7-fluorene)-alt-2,7-(9,9-dioctylfluorene))dibromide (PFN-Br)/quasi-2D HP/C_{60}/Bathocuproine (BCP)/Ag is used. Figure 5c shows the current–voltage curves of the champion PVs employing the corresponding quasi-2D HP films. Without any optimizations, the quasi-2D HP film designed by Gated-GPBO demonstrates the highest PV performance with a PCE of 11.16%, showing ≈15–60% enhancements compared to the performances of PV with NMF-predicted films (Detailed PV parameters are

summarized in Table S1, Supporting Information). Such a higher PCE of the Gated-GPBO-designed PV is majorly gained by the improvements in open-circuit voltage (V_{OC}) and fill factor (FF). With the substantial reduction of E_u (25.5 meV) in the Gated-GPBO-designed film, these results clearly demonstrate that the carrier loss is greatly suppressed in the Gated-GPBO-designed film, likely attributed to better chemical homogenization of the quasi-2D HP lattice. It should be noted that the films are synthesized at a low annealing temperature (95 °C), without any dedicated efforts in additional chemical and device engineering. This indicates that the Gated-GPBO-designed quasi-2D HP still has the potential to realize high performances, on par with those of widely used large-bandgap sub-cells that are required for tandem applications.[48]

Figure 5d,e and Figure S24 (Supporting Information) exhibit statistical distributions of PV parameters (PCE, V_{OC}, and J_{SC} and FF, respectively) for each PV configuration – estimated from 20 individual devices, obviously showing that the PV performances are reproducible. These results also validate the effectiveness of the Gated-GPBO for materials design used in this study, which can significantly accelerate the discovery of new functional materials realizing high PV performances from massive complex materials space.

2.4. Outlook

In summary, we systematically explore the chemical space of the Cs-based quasi-2D HPs – defined by the spacer cations – that determines their phase complexity by implementing high-throughput automated experimental workflow. Through high-throughput PL spectroscopy and ML-based data analysis, several key features are observed. The RP-type molecular spacers with high molecular weights exhibit slow crystallization dynamics, thus manifesting the growth of 3D-like HP phases – more stable than the pure 3D $CsPbI_3$ counterpart. The DJ-type spacer exhibits stronger chemical interactions between the spacers and inorganic building blocks, which is maintained during the overall crystallization sequence – starting from top to bottom. The resulting quasi-2D HP matrices mitigate vertical phase inhomogeneities, although the films exhibit poor stability and the non-HP δ-$CsPbI_3$ crystallites are evolved. It is found that the molecular geometry of the spacer plays a crucial role in realizing the stable quasi-2D HP lattices. The spacers with homocyclic, phenyl groups (PEA and DPA) exhibit a geometrically symmetric spacer–precursor interaction, which renders stable 3D-like HPs effectively protected by the aromatic rings. In contrast, the spacer with heterocyclic ring (ThEA) manifests asymmetric chemical interaction in the precursor state. This renders an upright molecular geometry at the 3D-like HP surface that cannot protect the lattice against O_2 or H_2O, thereby resulting in poor phase stability. These observations reveal the distinctive working principles of the spacer cations in the corresponding crystallization mechanisms, which have not been systematically identified so far. Thus, our findings provide new insights into the selection principles of molecular spacers for designing quasi-2D HPs.

To exploit the beneficial effects of molecular spacers – homogenizing vertical phase distribution and achieving high phase stability, the BDA and PEA-based ternary-composition quasi-2D HP system is explored. Here, we develop and deploy an active learning algorithm, a Gated-GPBO-based compositional exploration workflow. This allows for iterative discovery of specific compositions realizing target functionalities from a discrete chemical space of the molecular spacers in quasi-2D HPs, where the classical BO cannot achieve it. The quasi-2D HP film, with compositionally tailored by the Gated-GPBO indeed demonstrates the suited bandgaps and high PV performances, exhibiting promising functionalities and manufacturability for tandem PV applications. This work presents an effective experimental data-driven experimental workflow, which realizes bespoke design of optoelectronic functionalities and thus, substantially accelerates materials discovery for sustainable applications.

3. Experimental Section

High-Throughput Automated Synthesis and Optical Characterization: Stoichiometric 2D A_2PbI_4 (A = BA,ThEA, PEA, and DPA) or $A'PbI_4$ (A′ = BDA), and 3D $CsPbI_3$ precursor endmembers in DMF: DMSO solution (9:1, 0.4 M) were prepared by dissolving the materials in an N_2 glove box. These solutions were stirred overnight at room temperature and then transferred to a pipetting robot system (Opentrons, OT-2) in the N_2-purged box.

An experimental workflow was implemented for high-throughput robotic synthesis, according to the previous reports.[13,14,26–29] By using a 300 µL-capacity single-channel pipet, 2D and 3D endmember solutions were combinatorially mixed to achieve 50 µL of quasi-2D binary or ternary precursor mixtures with the designed compositional ratio for each well. Separately, the glass substrates, after sequential washing with acetone and isopropyl alcohol, were exposed to UV/O_3-treatment for 20 min. Then, the substrates were quickly transferred to the chamber for the pipetting robot system. For film fabrication, 0.5 µL of the prepared solutions were drop-casted onto the UV/O_3-treated glass substrates, which were already heated to 95 °C by using a heating module. The droplets of quasi-2D HP precursors were then crystallized at 95 °C for 10 min.

The synthesized quasi-2D HP film arrays were quickly mounted to a multi-mode optical reader (BioTek, Cytation 5) and time-evolved PL spectra of each film (1 nm step size) were collected alternatively at the top and bottom of the film surface, using 365 nm excitation beam. The emission spectra from each film spot were obtained as one "read cycle" every 15 mins for 96 films. The read cycle was repeated for 10 h. A PL read sequence was designed for the alternating scan of both the top and bottom surface, obtaining the time-evolved PL spectra from both the top and bottom over time. This resulted in the actual time interval between the read cycles at each position being 30 min. In Gen5 software, the spot size of the excitation beam was adjusted to be <3 mm in diameter, allowing for confining the excited area in each film. This not only suppressed the emission crosstalk caused from the neighboring films but also excluded undesired characterization of the edge of the film that could have different phase constitutions.

NMF Deconvolutions for PL Datasets: NMF data analysis was performed on Google Colab using Python 3.6 and the scikit-learn 0.22.1 library. The codes are available in the following link (Google Colab):
https://drive.google.com/file/d/1HzfvqLHVUY-WvPvLCO1Vrpxt2bVUE6wC/view?usp=drive_link
https://drive.google.com/file/d/1YgGM5jA9OcQP0Ic64HjIYPYbYOHqmyGB/view?usp=drive_link
https://drive.google.com/file/d/1Eg_uzc5PYnkOPfP0iQSsKfSiHVloBNgV/view?usp=drive_link
https://drive.google.com/file/d/1sTuCKfkoPqn3l-O_srCbQQ_mc9RZLhyY/view?usp=drive_link
https://drive.google.com/file/d/1rn-RZCq9ra4uzP3CK5fnhxptBYEGwOMy/view?usp=drive_link

https://drive.google.com/file/d/1t3b9HmpTyXYdY73LzwjngmXAyl5DQmRK/view?usp=drive_link

Gated Gaussian Process (GP) Bayesian Optimization (BO): The gated-GPBO approach leveraged two GP models to optimize experimental exploration by dynamically refining the search space based on complementary insights. In this work, the primary GPBO was tasked with maximizing PL intensity; an additional Gate-GP operated in tandem with the primary GP, focusing on actively refining the compositional space by evaluating the "instability score" derived from the temporal evolution of PL spectra. As the Gate-GP identified compositions with higher instability scores, it provided feedback to the primary GP, guiding it away from these compositions and toward compositional space where likely led to both high PL intensity and good stability. The notebook of the Gated-GPBO-driven exploration is publicly available at https://github.com/SLKS99/Automated-Discovery-and-Optimization-of-Molecular-Spacers-in-Cs–Based-Quasi-2D-Perovskites, allowing readers to adapt and deploy gated-GPBO in various experiments.

Materials Characterizations: Hyperspectral CL microscopy was conducted by using an environmental SEM instrument (FEI, Quattro) with a Delmic Sparc CL collection module. A parabolic mirror was utilized to collect the CL signals upon e-beam excitation. An e-beam with an acceleration voltage of 5 kV (beam current of 28 pA), with an acquisition time of 100 ms was used. A square pixel with a size of 100 × 100 nm^2 was used. All measurements were conducted in a low vacuum environment of 0.02 Torr with H_2O vapor, which effectively alleviated sample charging while minimizing e-beam-induced damage.

2D GIWAXS measurements were carried out at the 9A beamline (U-SAXS) at the Pohang Accelerator Laboratory in Pohang, Republic of Korea. The beam energy used was 11.07 KeV. Three different incidence angles, 0.1°, 0.2°, and 0.5° were used to explore the depth-dependent crystallographic properties of the quasi-2D HP films.

Solution phase ^{1}H NMR spectra were collected by a 400 MHz NMR spectrometer (Bruker, Avance III HD), with DMSO-d_6 as a solvent.

Solar Cell Fabrication and Characterization: For PV device fabrication, ITO substrates were cleaned in deionized water (DI water), acetone, and 2-propanol by ultrasonic treatment for 10 min each. After drying the substrates in an oven, the ITO substrates were treated with UV/O_3 for 20 min and then transferred to an N_2 glovebox. Subsequently, PTAA (1.5 mg ml^{-1} in Tol) was spin-coated on ITO at 3000 rpm for 30 s and annealed at 100 °C for 10 min. The perovskite precursor with a concentration of 1.0 M was prepared by mixing CsI, AI (A = BA, ThEA, PEA, and DPA), $BDAI_2$ and PbI_2 according to the composition ratio of $CsPbI_3$, A_2PbI_4, $BDAPbI_4$ in a mixed solution of DMF and DMSO (3:1 v/v). Before the perovskite spin-coating, the substrates were pre-heated at 60 °C for better wettability and crystallization. The perovskite precursor was spin-coated at 2000 rpm for 20 s and annealed at 100 °C for 10 min. After cooling down to room temperature, the substrate was transferred to a vacuum chamber and C_{60} (30 nm), BCP (7 nm), and Ag (100 nm) were sequentially deposited on the perovskite film under a pressure of $\approx 10^{-6}$ torr.

The *J–V* curves of the PV devices were measured in an N_2 glove box using a solar simulator (Newport-Oriel 94083A, Class AAA) synchronized with a Keithley source meter 2400. The light intensity was calibrated to 100 mW cm^{-2} using an NREL-certified Si-reference cell. To restrict the active cell area to 0.0314 cm^2, the PSCs of a specific size were masked using a shadow metal mask.

Supporting Information

Supporting Information is available from the Wiley Online Library or from the author.

Acknowledgements

M.U., S.L.S., and H.S. contributed equally to the work. M.A. and S.L.S. acknowledge support from the National Science Foundation (NSF), Award Number No. 2043205, and Alfred P. Sloan Foundation (Award No. FG-2022-18275). S.L.S. acknowledges partial support from the Center of Materials Processing (CMP), a Tennessee Higher Education Commission (THEC) supported Accomplished Center of Excellence. M.U. and J.Y. acknowledge support from the Yonsei University Research Fund of 2024-22-0106. This research was supported by the Global – Learning and Academic Research Institution for Master's. Ph.D. students and Postdocs (LAMP) Program of the National Research Foundation of Korea (NRF) grant funded by the Ministry of Education (No. RS-2024-00442483). The hyperspectral CL microscopy and Gated-GPBO development were supported by the Center for Nanophase Materials Sciences (CNMS), which is a US Department of Energy, Office of Science User Facility at Oak Ridge National Laboratory. This research was supported by the BrainLink program (NRF-2022H1D3A3A01077343) through the National Research Foundation of Korea (NRF) funded by Ministry of Science and ICT. This work was also supported by the National Research Foundation of Korea (NRF-2022R1A2C1002764), and the grant funded by the korea government (MSIT) (RS-2024-00436187). H.S. and M.U. respectively acknowledge support from the Basic Science Research Program through the National Research Foundation of Korea (NRF), funded by the Ministry of Education (RS-2023-00276169 and RS-2024-00463909). [Correction added on February 1, 2025, after first online publication: Funding information in the Acknowledgments section has been updated.]

Conflict of Interest

The authors declare no conflict of interest.

Data Availability Statement

The data that support the findings of this study are available from the corresponding author upon reasonable request.

Keywords

Bayesian optimization, high-throughput automated synthesis, machine learning, phase complexities, quasi-2D perovskites

Received: October 8, 2024
Revised: November 25, 2024
Published online:

[1] J. Lim, N. G. Park, S. I. Seok, M. Saliba, *Energy Environ. Sci.* **2024**, *17*, 4390.
[2] R. Lin, Y. Wang, Q. Lu, B. B. Tang, J. Li, H. Gao, Y. Gao, H. Li, C. Ding, J. Wen, P. Wu, C. Liu, S. Zhao, K. Xiao, Z. Liu, C. Ma, Y. Deng, L. Li, F. Fan, H. Tan, *Nature* **2023**, *620*, 994.
[3] R. Lin, J. Xu, M. Wei, Y. Wang, Z. Qin, Z. Liu, J. Wu, K. Xiao, B. Chen, S. M. Park, G. Chen, H. R. Atapattu, K. R. Graham, J. Xu, J. Zhu, L. Li, C. Zhang, E. H. Sargent, H. Tan, *Nature* **2022**, *603*, 73.
[4] H. Song, J. Yang, S. G. Lim, J. Lee, W. H. Jeong, H. Choi, J. H. Lee, H. Y. Kim, B. R. Lee, H. Choi, *Chem. Eng. J.* **2023**, *454*, 140224.
[5] Y. Hassan, J. H. Park, M. L. Crawford, A. Sadhanala, J. Lee, J. C. Sadighian, E. Mosconi, R. Shivanna, E. Radicchi, M. Jeong, C. Yang, H. Choi, S. H. Park, M. H. Song, F. De Angelis, C. Y. Wong, R. H. Friend, B. R. Lee, H. J. Snaith, *Nature* **2021**, *591*, 72.
[6] S. Li, Z. Zheng, J. Ju, S. Cheng, F. Chen, Z. Xue, L. Ma, Z. Wang, *Adv. Mater.* **2024**, *36*, 2307701.
[7] J. A. Steele, H. D. Jin, I. Dovgaliuk, R. F. Berger, T. Braeckevelt, H. F. Yuan, C. Martin, E. Solano, K. Lejaeghere, S. M. J. Rogge, C.

Notebaert, W. Vandezande, K. P. F. Janssen, B. Goderis, E. Debroye, Y. K. Wang, Y. T. Dong, D. X. Ma, M. Saidaminov, H. R. Tan, Z. H. Lu, V. Dyadkin, D. Chernyshov, V. Van Speybroeck, E. H. Sargent, J. Hofkens, M. B. J. Roeffaers, *Science* **2019**, *365*, 679.

[8] A. Swarnkar, A. R. Marshall, E. M. Sanehira, B. D. Chernomordik, D. T. Moore, J. A. Christians, T. Chakrabarti, J. M. Luther, *Science* **2016**, *354*, 92.

[9] X. Li, J. M. Hoffman, M. G. Kanatzidis, *Chem. Rev.* **2021**, *121*, 2230.

[10] C. M. M. Soe, G. P. Nagabhushana, R. Shivaramaiah, H. H. Tsai, W. Y. Nie, J. C. Blancon, F. Melkonyan, D. H. Cao, B. Traoré, L. Pedesseau, M. Kepenekian, C. Katan, J. Even, T. J. Marks, A. Navrotsky, A. D. Mohite, C. C. Stoumpos, M. G. Kanatzidis, *Proc. Natl. Acad. Sci. U. S. A.* **2019**, *116*, 58.

[11] L. N. Quan, M. Yuan, R. Comin, O. Voznyy, E. M. Beauregard, S. Hoogland, A. Buin, A. R. Kirmani, K. Zhao, A. Amassian, D. H. Kim, E. H. Sargent, *J. Am. Chem. Soc.* **2016**, *138*, 2649.

[12] J. W. Lee, Z. Dai, T. H. Han, C. Choi, S. Y. Chang, S. J. Lee, N. De Marco, H. Zhao, P. Y. Sun, Y. Huang, Y. Yang, *Nat. Commun.* **2018**, *9*, 3021.

[13] J. Yang, B. J. Lawrie, S. V. Kalinin, M. Ahmadi, *Adv. Energy Mater.* **2023**, *13*, 2302337.

[14] J. Yang, J. Hidalgo, D. Song, S. V. Kalinin, J. P. Correa-Baena, M. Ahmadi, *Adv. Funct. Mater.* **2024**, *34*, 2409293.

[15] N. J. Jeon, J. H. Noh, Y. C. Kim, W. S. Yang, S. Ryu, S. I. Seok, *Nat. Mater.* **2014**, *13*, 897.

[16] H. Song, H. B. Kim, S. C. Cho, J. Lee, J. Yang, W. H. Jeong, J. Y. Won, H. I. Jeong, J. Yeop, J. Y. Kim, B. J. Lawrie, M. Ahmadi, B. R. Lee, M. Kim, S. J. Choi, D. S. Kim, M. Lee, S. U. Lee, Y. Jo, H. Choi, *Joule* **2024**, *8*, 2283.

[17] A. D. Taylor, Q. Sun, K. P. Goetz, Q. An, T. Schramm, Y. Hofstetter, M. Litterst, F. Paulus, Y. Vaynzof, *Nat. Commun.* **2021**, *12*, 1878.

[18] J. Hidalgo, L. Atourki, R. Li, A. F. Castro-Méndez, S. Kim, E. A. Sherman, A. S. Bieber, M. J. Sher, L. Nienhaus, C. A. R. Perini, J. P. Correa-Baena, *Mater. Today* **2023**, *68*, 13.

[19] L. Kuai, J. Li, Y. Li, Y. Wang, P. Li, Y. Qin, T. Song, Y. G. Yang, Z. Chen, X. Gao, B. Sun, *ACS Energy Lett.* **2020**, *5*, 8.

[20] C. A. R. Perini, E. Rojas-Gatjens, M. Ravello, A. F. Castro-Mendez, J. Hidalgo, Y. An, S. Kim, B. Lai, R. Li, C. Silva-Acuña, J. P. Correa-Baena, *Adv. Mater.* **2022**, *34*, 2204726.

[21] M. A. Hope, T. Nakamura, P. Ahlawat, A. Mishra, M. Cordova, F. Jahanbakhshi, M. Mladenovic, R. Runjhun, L. Merten, A. Hinderhofer, B. I. Carlsen, D. J. Kubicki, R. Gershoni-Poranne, T. Schneeberger, L. C. Carbone, Y. Liu, S. M. Zakeeruddin, J. Lewinski, A. Hagfeldt, F. Schreiber, U. Rothlisberger, M. Grätzel, J. V. Milic, L. Emsley, *J. Am. Chem. Soc.* **2021**, *143*, 1529.

[22] X. Zhao, M. L. Ball, A. Kakekhani, T. Liu, A. M. Rappe, Y. L. Loo, *Nat. Commun.* **2022**, *13*, 3970.

[23] K. Wang, Z. Y. Lin, Z. Zhang, L. Jin, K. Ma, A. H. Coffey, H. R. Atapattu, Y. Gao, J. Y. Park, Z. Wei, B. P. Finkenauer, C. Zhu, X. Meng, S. N. Chowdhury, Z. Chen, T. Terlier, T. H. Do, Y. Yao, K. R. Graham, A. Boltasseva, T. F. Guo, L. Huang, H. Gao, B. M. Savoie, L. Dou, *Nat. Commun.* **2023**, *14*, 397.

[24] S. L. Sanchez, Y. Tang, B. Hu, J. Yang, M. Ahmadi, *Matter* **2023**, *6*, 2900.

[25] J. Zhang, J. Wu, S. Langner, B. Zhao, Z. Xie, J. A. Hauch, H. A. Afify, A. Barabash, J. Luo, M. Sytnyk, W. Meng, K. Zhang, C. Liu, A. Osvet, N. Li, M. Halik, W. Heiss, Y. Zhao, C. J. Brabec, *Adv. Funct. Mater.* **2022**, *32*, 2207101.

[26] K. Higgins, S. M. Valleti, M. Ziatdinov, S. V. Kalinin, M. Ahmadi, *ACS Energy Lett.* **2020**, *5*, 3426.

[27] K. Higgins, M. Ziatdinov, S. V. Kalinin, M. Ahmadi, *J. Am. Chem. Soc.* **2021**, *143*, 19945.

[28] J. Yang, A. S. Fuhr, K. M. Roccapriore, B. Dryzhakov, B. Hu, B. G. Sumpter, S. V. Kalinin, M. Ahmadi, *Ligand-Induced Self-Assembly of Twisted 2D Halide Perovskites*, ChemRxiv **2024**.

[29] E. Foadian, J. Yang, S. B. Harris, Y. Tang, C. M. Rouleau, S. Joy, K. R. Graham, B. J. Lawrie, B. Hu, M. Ahmadi, *Adv. Funct. Mater.* **2024**, 2411164.

[30] H. Song, J. Yang, W. H. Jeong, J. Lee, T. H. Lee, J. W. Yoon, H. Lee, A. J. Ramadan, R. D. J. Oliver, S. C. Cho, S. G. Lim, J. W. Jang, Z. K. Yu, J. T. Oh, E. D. Jung, M. H. Song, S. H. Park, J. R. Durrant, H. J. Snaith, S. U. Lee, B. R. Lee, H. Choi, *Adv. Mater.* **2023**, *35*, 2209486.

[31] Y. Lin, Y. Fang, J. J. Zhao, Y. Shao, S. J. Stuard, M. M. Nahid, H. Ade, Q. Wang, J. E. Shield, N. Zhou, A. M. Moran, J. Huang, *Nat. Commun.* **2019**, *10*, 1008.

[32] S. Chen, X. Xiao, B. Chen, L. L. Kelly, J. Zhao, Y. Z. Lin, M. F. Toney, J. Huang, *Sci. Adv.* **2021**, *7*, abb2412.

[33] A. Dubey, S. L. Sanchez, J. Yang, M. Ahmadi, *Chem. Mater.* **2024**, *36*, 2165.

[34] J. Chen, Z. Zhai, Q. Liu, H. Zhou, *Nanoscale Horiz.* **2023**, *8*, 1628.

[35] T. Xiang, T. Li, M. Wang, W. Zhang, M. Ahmadi, X. Wu, T. F. Xu, M. Xiao, L. Xu, P. Chen, *Nano Energy* **2022**, *95*, 107000.

[36] C. H. Chen, C. H. Hsu, I. C. Ni, B. H. Lin, C. I. Wu, C. C. Kuo, C. C. Chueh, *Nanoscale* **2022**, *14*, 17409.

[37] S. Peng, Z. Miao, Y. Liang, R. Zhao, F. Yuan, H. Zhu, W. Liang, Y. Shi, P. Li, Y. Zhang, Y. Song, *Matter* **2024**, *7*, 3500.

[38] L. Kong, X. Zhang, Y. Li, H. Wang, Y. Jiang, S. Wang, M. You, C. Zhang, T. Zhang, S. V. Kershaw, W. Zheng, Y. Yang, Q. Lin, M. Yuan, A. L. Rogach, X. Yang, *Nat. Commun.* **2021**, *12*, 1246.

[39] X. Zhang, R. Munir, Z. Xu, Y. Liu, H. Tsai, W. Nie, J. Li, T. Niu, D. M. Smilgies, M. G. Kanatzidis, A. D. Mohite, K. Zhao, A. Amassian, S. Liu, *Adv. Mater.* **2018**, *30*, 1707166.

[40] Q. Wang, X. Zheng, Y. Deng, J. Zhao, Z. Chen, J. Huang, *Joule* **2017**, *1*, 371.

[41] D. K. Lafollette, J. Hidalgo, O. Allam, J. H. Yang, A. Shoemaker, R. P. Li, B. R. Y. Lai, B. Lawrie, S. Kalinin, C. A. R. Perini, M. Ahmadi, S. S. Jang, J. P. Correa-Baena, *J. Am. Chem. Soc.* **2024**, *146*, 18576.

[42] J. Yang, D. K. LaFollette, B. J. Lawrie, A. V. Ievlev, Y. Liu, K. P. Kelley, S. V. Kalinin, J. P. Correa-Baena, M. Ahmadi, *Adv. Energy Mater.* **2023**, *13*, 2302337.

[43] K. Ho, M. Wei, E. H. Sargent, G. C. Walker, *ACS Energy Lett.* **2021**, *6*, 934.

[44] S. Yu, Y. Yan, M. Abdellah, T. Pullerits, K. Zheng, Z. Liang, *Small* **2019**, *15*, 1905081.

[45] G. Wu, T. Liu, M. Hu, Z. Zhang, S. L. Li, L. Xiao, J. Guo, Y. Wang, A. Zhu, W. Li, H. Zhou, Y. Zhang, R. F. Chen, G. Xing, *Adv. Mater.* **2023**, *35*, 2303061.

[46] H. Guthrey, J. Moseley, *Adv. Energy Mater.* **2020**, *10*, 1903840.

[47] F. Deschler, M. Price, S. Pathak, L. E. Klintberg, D. D. Jarausch, R. Higler, S. Hüttner, T. Leijtens, S. D. Stranks, H. J. Snaith, M. Atatüre, R. T. Phillips, R. H. Friend, *J. Phys. Chem. Lett.* **2014**, *5*, 1421.

[48] H. Chen, A. Maxwell, C. Li, S. Teale, B. Chen, T. Zhu, E. Ugur, G. Harrison, L. Grater, J. Wang, Z. Wang, L. Zeng, S. M. Park, L. Chen, P. Serles, R. A. Awni, B. Subedi, X. Zheng, C. Xiao, N. J. Podraza, T. Filleter, C. Liu, Y. Yang, J. M. Luther, S. De Wolf, M. G. Kanatzidis, Y. Yan, E. H. Sargent, *Nature* **2023**, *613*, 676.